

Supporting Information for

Evaluation of Electrochemical Properties of Nanostructured Metal Oxide Electrodes

Immersed in Redox-Inactive Organic Media

David A. Brewster,^a Melissa D. Koch,^a Kathryn E. Knowles*

Department of Chemistry, University of Rochester, Rochester, NY 14627

*e-mail: kknowles@ur.rochester.edu, ^aD.A.B. and M.D.K. contributed equally to this work

Table of Contents	Page #
Characterization Methods	S2-3
Figure S1 – Bode-Phase Plot Simulation for Circuit A	S4
Table S1 – Tabulated Values for Simulated Bode-Phase Plots	S5
Figure S2 – Effect of Increasing Film Thickness on Impedance Measurements	S6
Figure S3 – Metal Oxide Powder X-Ray Diffraction	S6
Figure S4 – Metal Oxide X-Ray Photoelectron Spectroscopy	S7
Figure S5 – Representative Scanning Electron Micrographs Electrochemically Deposited Films	S7
Figure S6 – Representative Transmission Electron Micrographs	S8
Figure S7 – Representative Lissajous plots obtained in acetonitrile	S8
Figure S8 – Representative Lissajous plots obtained in aqueous electrolyte	S9
Figure S9 – Representative Scanning Electron Micrographs of Deposited Films	S9
Figure S10 – Representative Bode Plots with Circuit Fits for NiO Films	S10
Figure S11 – Representative Bode Plots with Circuit Fits for α -Fe ₂ O ₃ Films	S11
Figure S12 – Representative $1/C_1^2$ plots overlaid with Bode plots for Nanoparticle Films on Pt	S12
Figure S13 – Representative Bode Plots for electrochemically deposited NiO	S13
Figure S14 – Representative $1/C_1^2$ plots overlaid with R_1 values for Metal Oxide Electrodes	S14
Figure S15 – Plots of $1/C_1^2$ for NiO films plotted from 0-1 V vs. NHE	S15
Figure S16 – Individual $1/C_1^2$ plots for NiO and α -Fe ₂ O ₃	S16
Figure S17 – Representative C_1 plots for NiO and α -Fe ₂ O ₃ films on Pt and Au	S17
Figure S18 – Cyclic Voltammograms of Metal Oxide Electrodes in 0.1 M TBAPF ₆ , dry Acetonitrile	S18
Figure S19 – Representative $1/C_1^2$ plots for NiO and α -Fe ₂ O ₃ Nanoparticles on Pt and Au	S19
Figure S20 – Representative Comparison of C_2 and N-Values for Metal Oxide and Bare Metal Electrodes	S20
Table S2 – Tabulated Values for Cyclic Voltammograms of Bare and Metal Oxide Electrodes	S21
Figure S21 – Cyclic Voltammograms of Ferrocene Collected with Bare and Metal Oxide Electrodes	S22
Figure S22 – Plots of R_2 vs. Applied Potential for Bare and Metal Oxide Electrodes with TBAPF ₆ and TMAPF ₆ electrolytes	S23

Table S3 - Average Values of R_2 Obtained from EIS Measurements of Various Electrodes	S23
Figure S23 – R_3 Dependence on Pathway	S24
Table S4 – Tabulated Values of R_3 for TBA and TMA at 10,000 Hz	S24
Figure S24 – Representative Nyquist Plots at Varied Electrolyte Concentrations	S25
Table S5 – Tabulated Values of R_3 for Varied Electrolyte Concentrations	S25
Figure S25 – Interchangeability of R_A/R_B and C_A/C_B in Circuit C	S26
Figure S26 – Bode-Phase Plot Simulation for Circuit C, large R_C	S27
Figure S27 – Bode-Phase Simulation for Circuit C, Resolving Three Features	S28
Figure S28 – Representative Bode plots for NiO in water and acetonitrile	S29

Characterization Methods

Transmission Electron Microscopy (TEM). TEM images were taken using a FEI Tecnai F20 G2 (S)TEM with a beam energy of 200 kV. Samples were prepared for analysis by pipetting 2-3 drops of a dilute suspension of nanocrystals in hexane onto lacy carbon grids (Ted Pella 300 mesh Cu grid). The nanocrystal dimensions were measured using ImageJ software. For spherical NiO particles, the diameter was recorded. For cubic α - Fe_2O_3 the size of the nanocrystal was defined by the longest dimension visible in the TEM images. About 120 individual nanoparticles were measured for each sample to determine the average nanoparticle size.

Scanning Electron Microscopy (SEM). SEM images were taken with a Zeiss Auriga Scanning Electron Microscope. Films were analyzed as deposited and grounded to the instrument by copper tape contacting the underlying gold electrode.

Powder X-Ray Diffraction (p-XRD). p-XRD spectra of metal oxide samples were collected using Mo $K\alpha$ radiation ($\lambda = 0.71073 \text{ \AA}$) from a Rigaku XtaLAB Synergy-S Diffractometer. Nanocrystal samples were transferred directly to a nylon loop for analysis. For film samples, a small portion of the sample is carefully scraped from the film surface and transferred to a nylon loop for analysis. JCPDS references reporting signals from Cu $K\alpha$ radiation were converted with Bragg's law for direct comparison.

X-Ray Photoelectron Spectroscopy (XPS). XPS spectra were obtained on a Kratos AXIS Ultra DLD spectrophotometer. Scans were taken using an Al anode source with an emission current of 10 mA, an accelerating voltage of 15 kV, and a pass energy of 80 eV. Nanocrystal samples were prepared by drop-casting dilute solutions of nanocrystals onto cleaned Si wafers and grounded to the instrument using carbon tape. Nanocrystal samples were analyzed with the following neutralizer settings: 7 μA current, 5 V charge balance, and 1.3 V filament bias. Electrochemically

deposited films were grounded to the instrument *via* copper tape contacting the underlying gold electrode. Films samples were analyzed with neutralizer settings: 1.9 A current, 3.2 V charge balance, and 1.1 V filament bias. All region scan binding energies are corrected to C 1s at a binding energy of 284.8 eV. XPS measurements of α -Fe₂O₃ and NiO films were consistent with data reported previously for iron(III) oxides¹ and NiO,² respectively.

Measurement of peak current as a function of scan rate.

Cyclic voltammograms of ferrocene were collected with various voltage scan rates in an inert atmosphere using a standard 3-electrode set up comprising a metal oxide working electrode, Pt wire counter electrode, and a non-aqueous Ag|Ag⁺ reference electrode (BioLogic RE-7). The electrolyte consisted of 0.1 M tetrabutylammonium hexafluorophosphate (TBAPF₆) and 1 mM ferrocene in dry acetonitrile. The surface area of the electrode was calculated using the Randles-Sevcik equation (eq. S1) where n is the number of electrons transferred, F is the Faraday constant

$$i_p = 0.4463 nFAC \left(\frac{nFvD}{RT} \right)^{1/2} \quad (\text{S1})$$

in C mol⁻¹, A is the surface area of the electrode in cm², C is the concentration of ferrocene in mol cm⁻³, v is scan rate in V s⁻¹, D is the diffusion coefficient of ferrocene (reported in literature as 2.24×10^{-5} cm² s⁻¹ for 0.1 M TBAPF₆ in acetonitrile at room temperature³²), R is the ideal gas constant in J K⁻¹ mol⁻¹, and T is temperature in K.^{3,4}

Aqueous Electrochemical Impedance Measurements

Aqueous electrochemical impedance measurements were collected under argon atmosphere with a Ag|AgCl (3 M NaCl, Basi) reference electrode in a 0.1 M potassium phosphate (KP_i) buffer in Nanopure water. The pH of the electrolyte solution was 7.2 after it was purged with nitrogen and prior to use. EIS measurements were performed over the potential window -0.5 – 0.5 V vs. Ag|AgCl. To compare the aqueous measurements to the nonaqueous measurements, we convert potentials collected versus Ag|AgCl to RHE using equation S2 where $E^0(\text{Ag}|\text{AgCl}) = 0.197$ V versus NHE.³³ The RHE reference accounts for the pH dependent behavior of the metal oxide film when immersed in aqueous electrolyte. For completeness, we also report the applied potentials used in the aqueous measurements relative to NHE using equation S3 to perform the conversion.

$$E(\text{RHE}) = E(\text{Ag}|\text{AgCl}) + E^0(\text{Ag}|\text{AgCl}) + 0.059 \text{ pH} \quad (\text{S2})$$

$$E(\text{NHE}) = E(\text{Ag}|\text{AgCl}) + E^0(\text{Ag}|\text{AgCl}) \quad (\text{S3})$$

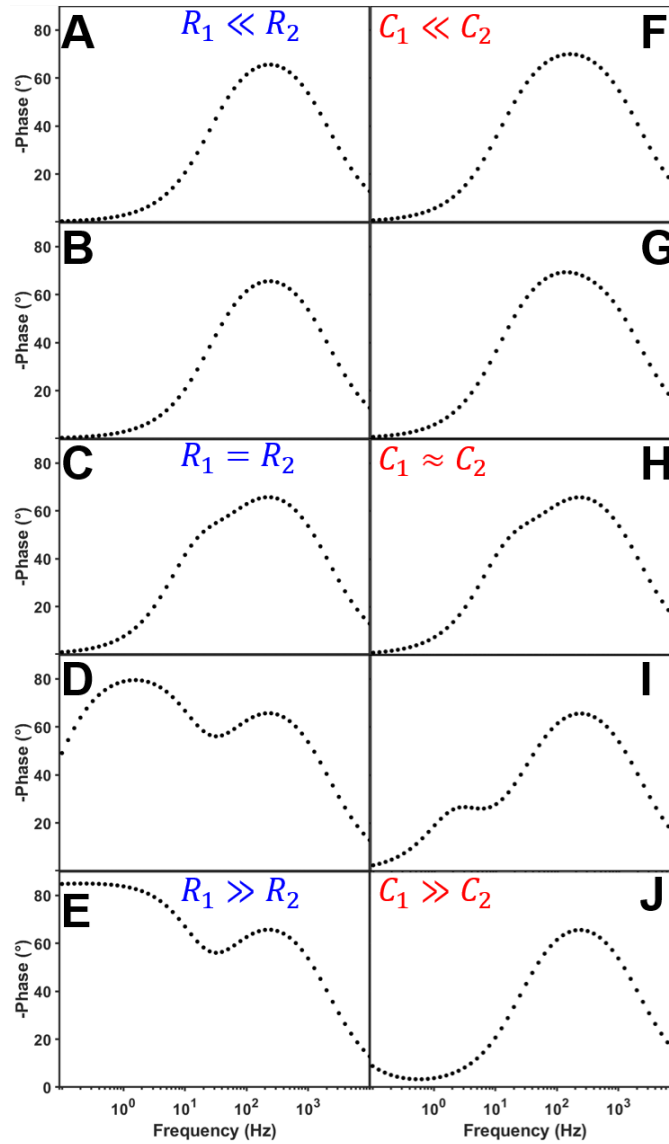


Figure S1. A-J) Simulated Bode-phase plots for model circuit A showing the impact of varying the relative intensities of C_1 , C_2 , R_1 , and R_2 . To provide a comparable model to our analysis, C_2 is modelled with a CPE with a constant N value of 0.9. Corresponding values of C_1 , C_2 , R_1 , and R_2 are provided in Table S1.

Table S1. Table of values corresponding to the simulated Bode-phase plots in Figure S1.

Plot	R₁ (Ω)	R₂ (Ω)	C₁ (F)	Q₂ (Ω^{-1})	N₂	C_{2, eff} (F)
A	1	1×10^4	1×10^{-6}	1×10^{-6}	0.9	6×10^{-7}
B	1×10^2	1×10^4	1×10^{-6}	1×10^{-6}	0.9	6×10^{-7}
C	1×10^4	1×10^4	1×10^{-6}	1×10^{-6}	0.9	6×10^{-7}
D	1×10^6	1×10^4	1×10^{-6}	1×10^{-6}	0.9	6×10^{-7}
E	1×10^8	1×10^4	1×10^{-6}	1×10^{-6}	0.9	6×10^{-7}
F	1×10^4	1×10^4	1×10^{-9}	1×10^{-6}	0.9	6×10^{-7}
G	1×10^4	1×10^4	1×10^{-7}	1×10^{-6}	0.9	6×10^{-7}
H	1×10^4	1×10^4	1×10^{-6}	1×10^{-6}	0.9	6×10^{-7}
I	1×10^4	1×10^4	1×10^{-5}	1×10^{-6}	0.9	6×10^{-7}
J	1×10^4	1×10^4	1×10^{-3}	1×10^{-6}	0.9	6×10^{-7}

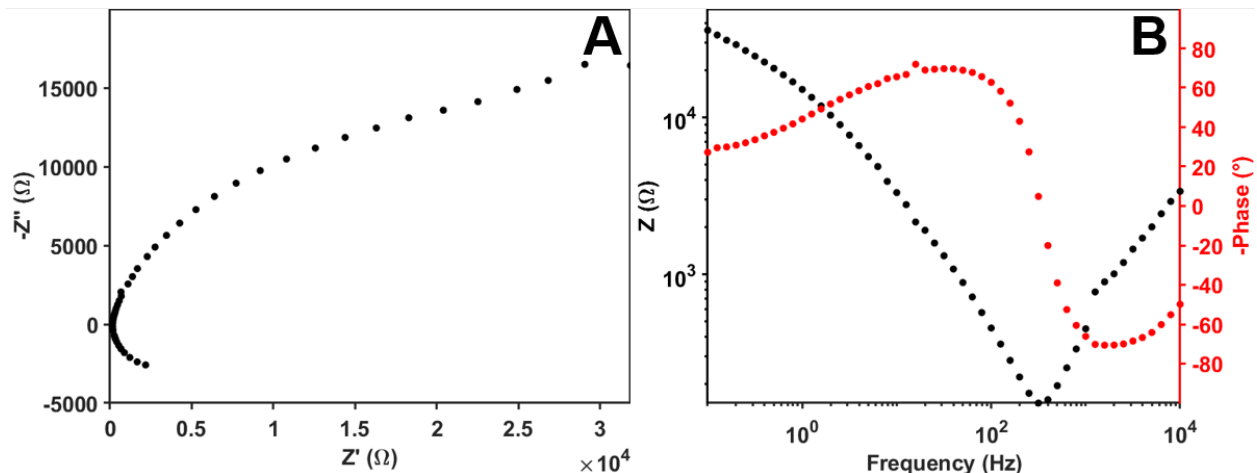


Figure S2. Nyquist (A) and Bode (B) plots resulting from the analysis of an $\alpha\text{-Fe}_2\text{O}_3$ film that was electrodeposited for 60 minutes (approximate thickness 470 nm). Data was collected in 0.1 M TBAPF₆ in dry acetonitrile at 1 V vs. Ag|AgCl.

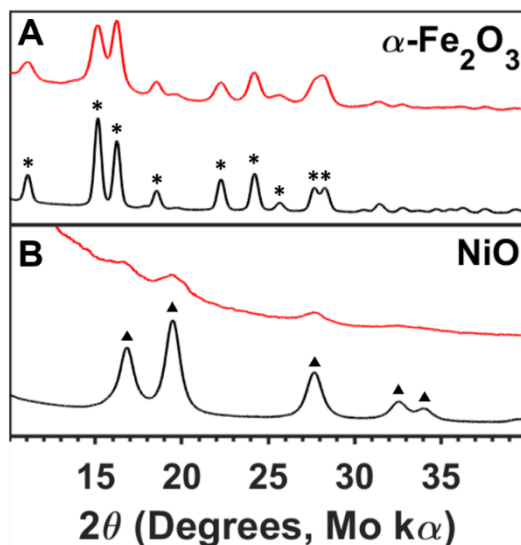


Figure S3. Powder X-ray diffraction patterns of A) $\alpha\text{-Fe}_2\text{O}_3$ and B) NiO nanocrystal (black traces) and film (red traces) samples. Crystal phase references are denoted by labels: triangle (▲) represents NiO (JCPD: 01-078-0643), asterisk (*) represents $\alpha\text{-Fe}_2\text{O}_3$ (JCPD: 33-664).

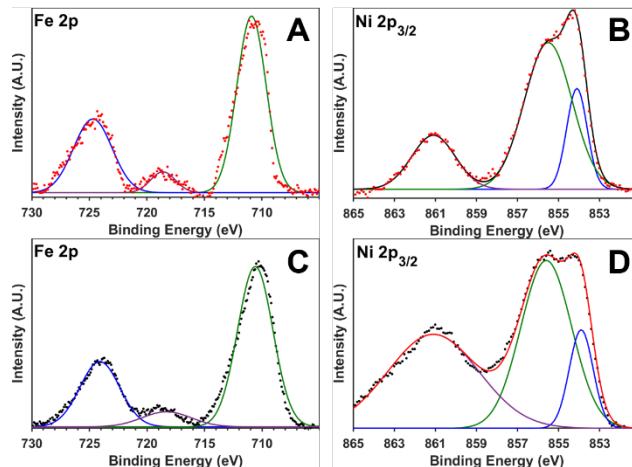


Figure S4. Representative X-ray photoelectron spectra collected for electrochemically deposited $\alpha\text{-Fe}_2\text{O}_3$ (A) and NiO (B) films and nanocrystalline $\alpha\text{-Fe}_2\text{O}_3$ (C) and NiO (D) films. The electrochemically deposited and nanocrystalline films of $\alpha\text{-Fe}_2\text{O}_3$ exhibit similar peaks for the Fe 2p region, with binding energies of 710.9 eV and 710.6 eV, respectively, for the Fe $2p_{3/2}$ peak. The electrochemically deposited and nanocrystalline films of NiO also exhibit similar peaks for the Ni $2p_{3/2}$ region, where fit results indicate binding energies of 853.7 and 855.2 eV for the electrochemically deposited film and 853.9 and 855.6 eV for the nanocrystalline film.

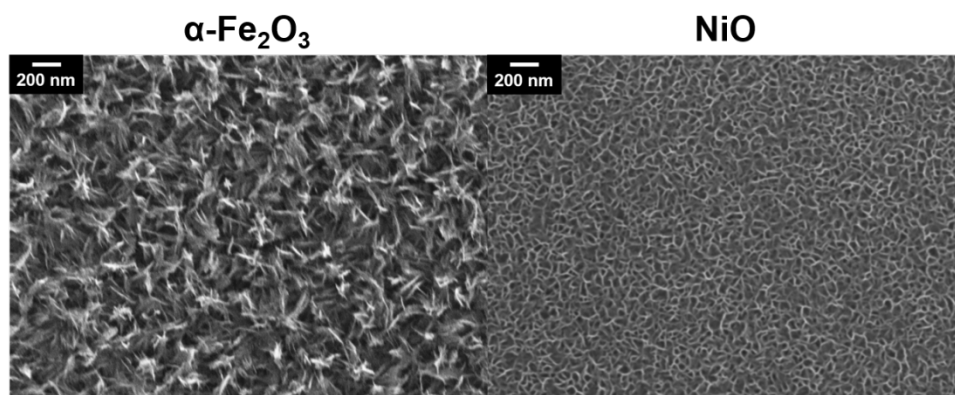


Figure S5. Representative SEM images of electrochemically deposited electrode films, each with a scale bar of 200 nm.

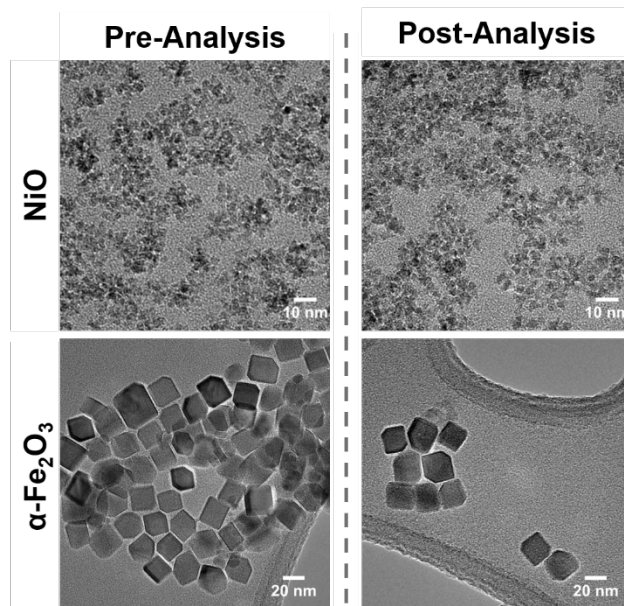


Figure S6. Representative transmission electron micrographs of NiO and α -Fe₂O₃ nanocrystals pre and post electrochemical analysis. These results indicate that upon electrochemical analysis nanocrystals remain relatively intact and do not degrade or corrode upon analysis.

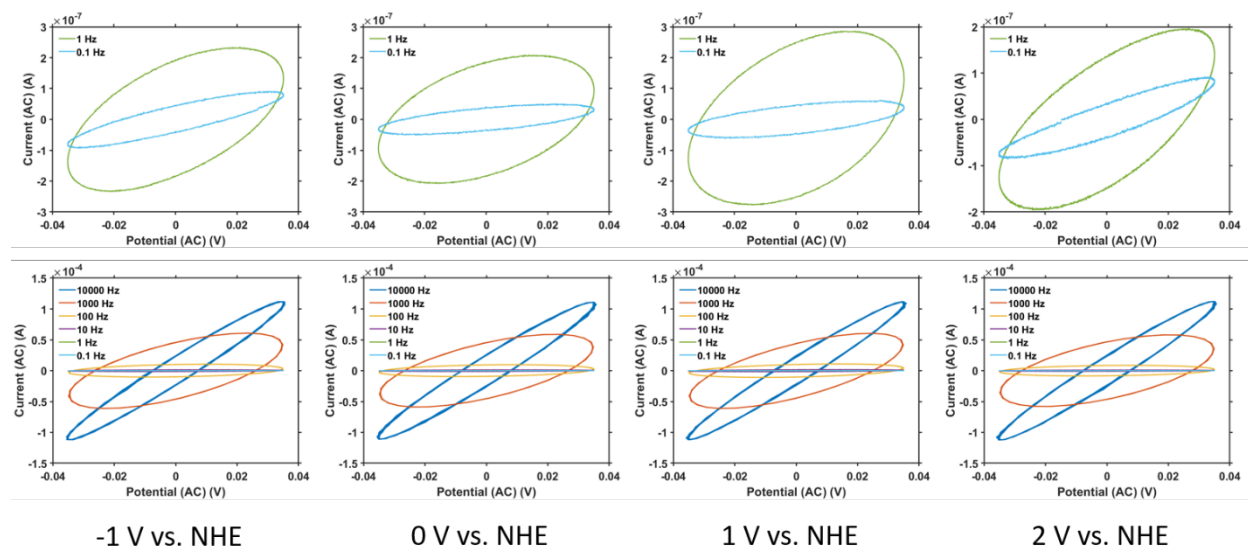


Figure S7. Representative Lissajous plots at varied potentials of NiO nanoparticles dropcast onto platinum disc as collected in 0.1 M TBAPF₆ in dry acetonitrile. Impedance data was collected with 25 mV amplitudes. All plots contain tilted ellipsoid indicating collected data is within the pseudo linear range for all frequencies and potentials.

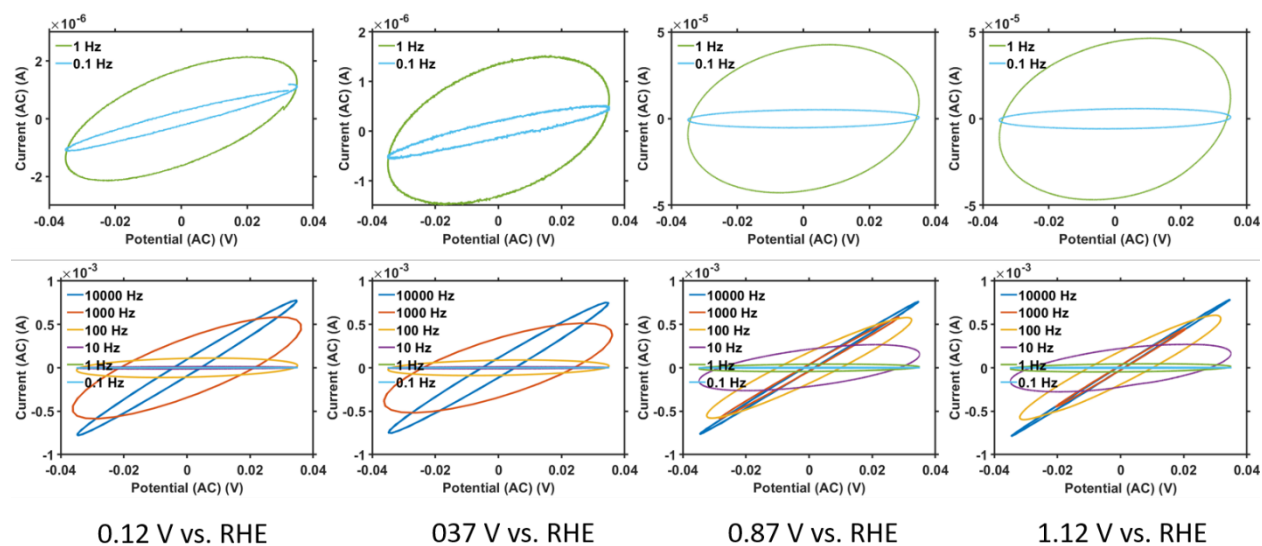


Figure S8. Representative Lissajous plots at varied potentials of an NiO film electrochemically deposited on gold as collected in pH 7.2, 0.1 M KPi in water. Impedance data was collected with 25 mV amplitudes. All plots contain tilted ellipsoid indicating collected data is within the pseudo linear range for all frequencies and potentials.

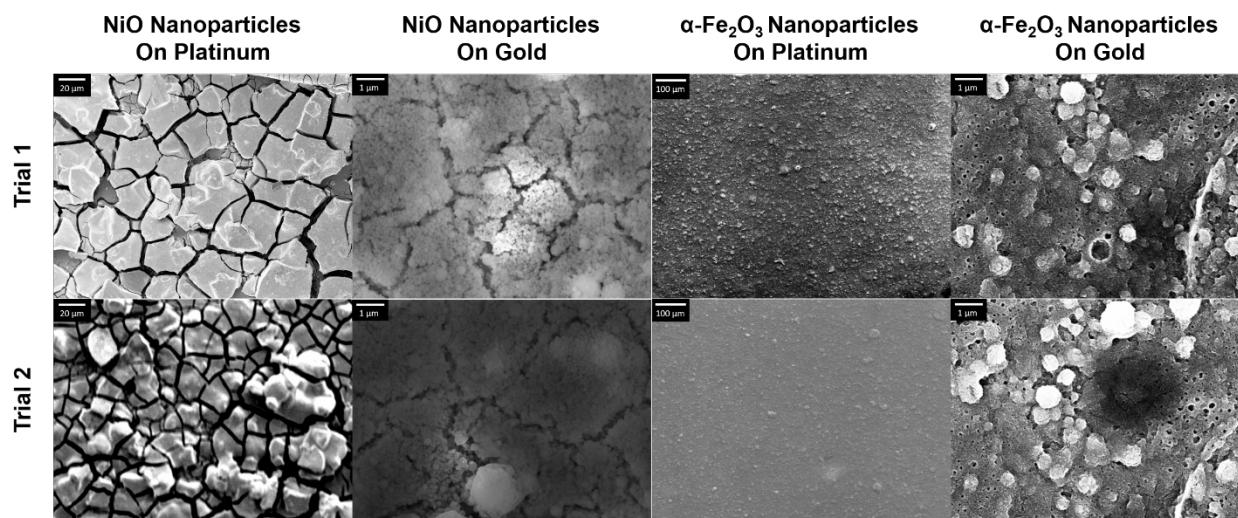


Figure S9. Representative scanning electron micrographs illustrating reproducible morphology between two trials (trial 1 *top*, trial 2 *bottom*) of films comprised of dropcast nanocrystals for NiO on Platinum (*left*), NiO on Gold (*middle-left*), α -Fe₂O₃ on Platinum (*middle-right*), and α -Fe₂O₃ on Gold (*right*).

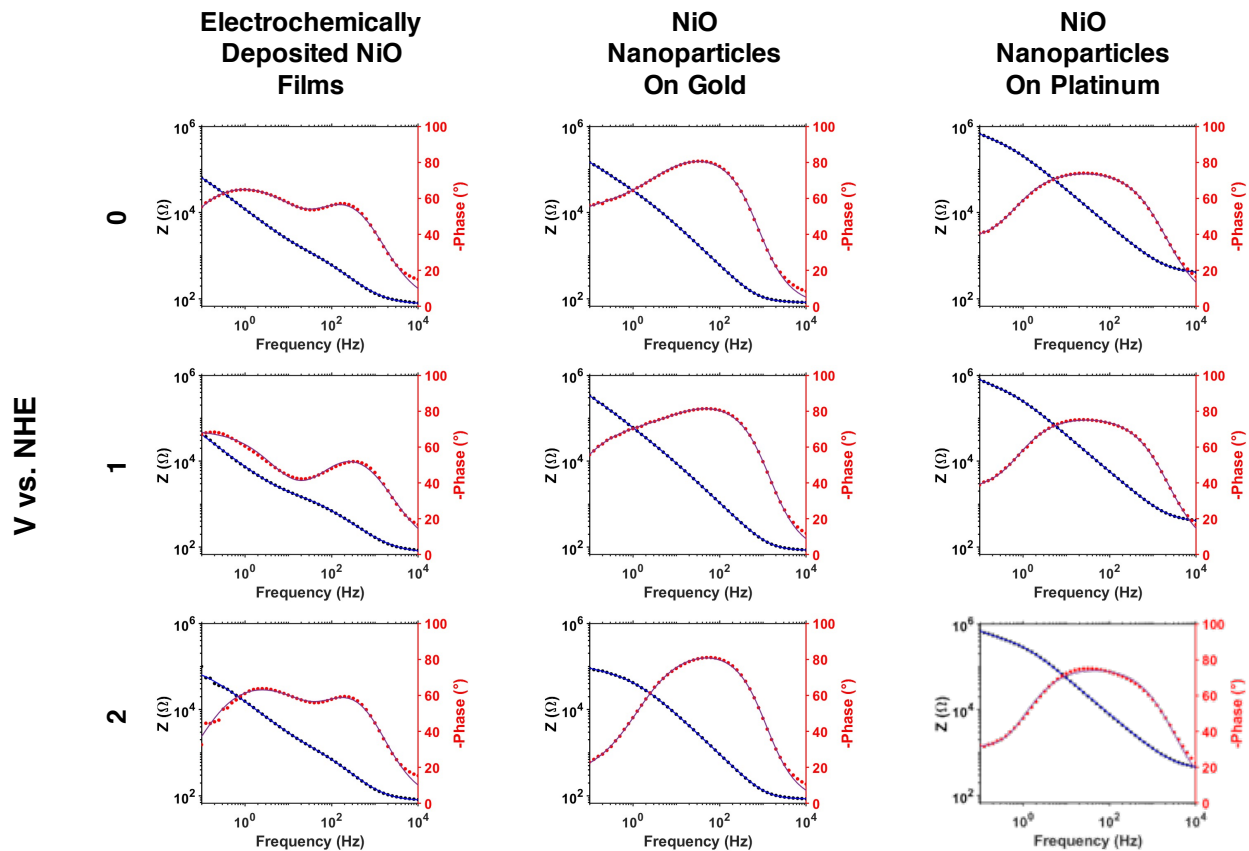


Figure S10. Representative fits of Bode plots collected for electrochemically deposited (*left*) and dropcast nanocrystal (*middle*) films of NiO on Au and a dropcast nanocrystal film of NiO on Pt (*right*). These data were collected at applied potentials of 0 (*top*), 1 (*middle*), and 2 (*bottom*) V vs. NHE and fit to model Circuit A from the main text using NOVA fitting software.

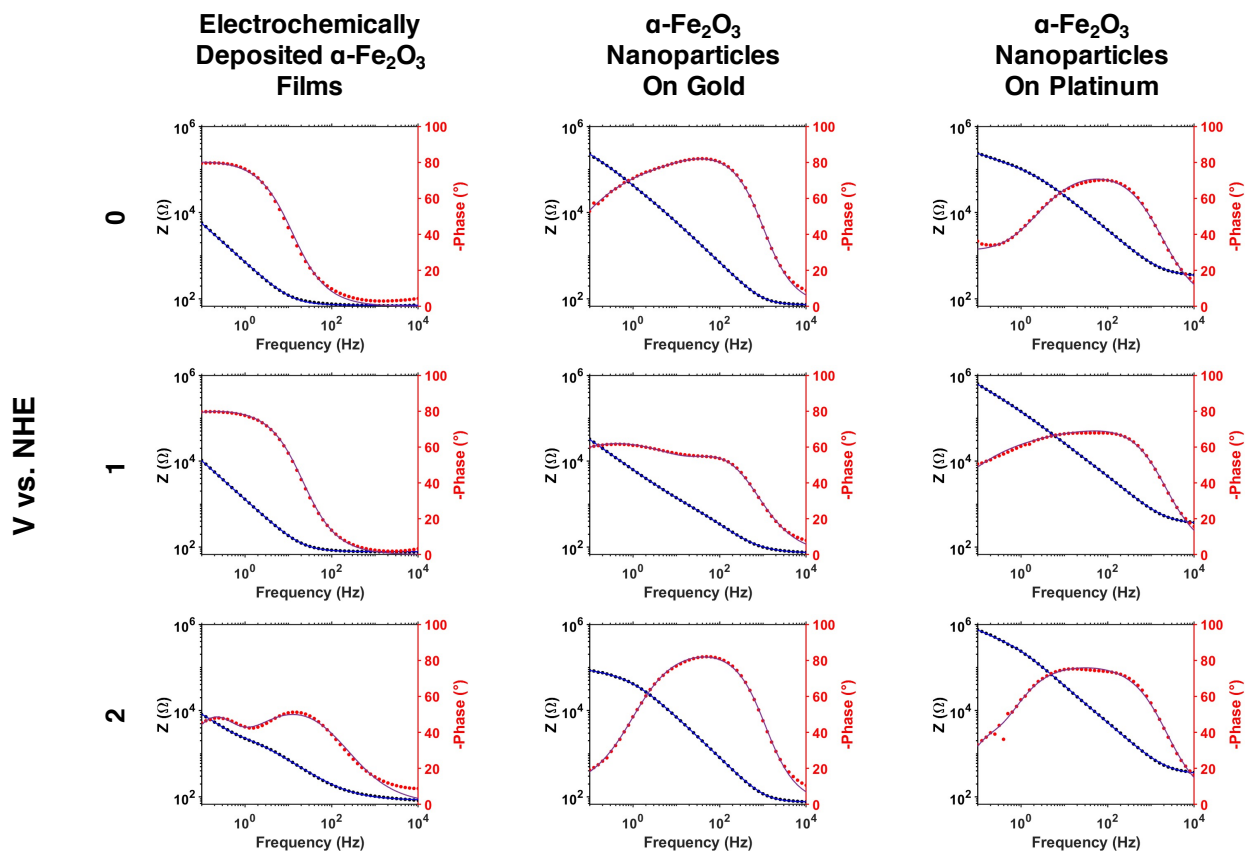


Figure S11. Representative fits of Bode plots collected for electrochemically deposited (*left*) and dropcast nanocrystal (*middle*) films of $\alpha\text{-Fe}_2\text{O}_3$ on Au and a dropcast nanocrystal film of $\alpha\text{-Fe}_2\text{O}_3$ on Pt (*right*). These data were collected at applied potentials of 0 (*top*), 1 (*middle*), and 2 (*bottom*) V vs. NHE. Dropcast nanocrystal films were fit to model Circuit A from the main text using NOVA fitting software at all potentials. For the electrochemically deposited $\alpha\text{-Fe}_2\text{O}_3$ film, the data collected at potentials more negative than 1.2 V vs. NHE (such as 0 and 1 V vs. NHE) fit best to model Circuit B, whereas data collected at more positive potentials (such as 2 V vs. NHE) fit best to model Circuit A.

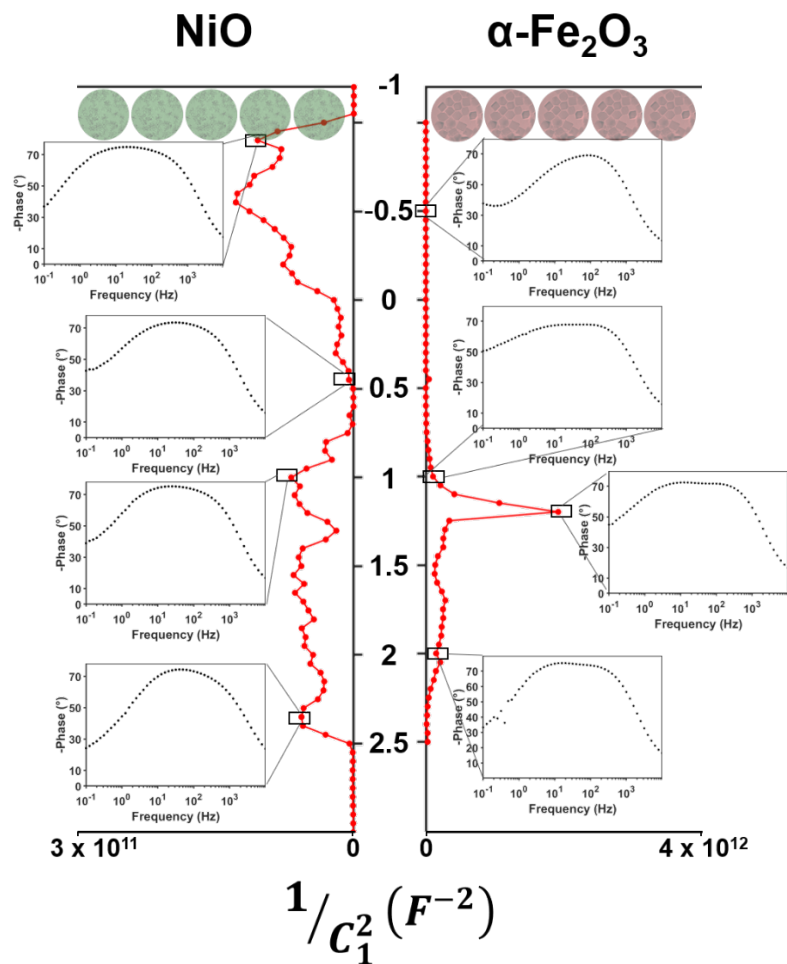


Figure S12. Representative plots of the inverse squared capacitance ($1/C_1^2$) versus applied potential for films of NiO (*left*) and α -Fe₂O₃ (*right*) nanocrystals dropcast on Pt. The insets contain images of Bode plots illustrating the dependence of phase angle on frequency and correspond to the potentials indicated by black boxes. All data was obtained in the presence of 0.1 M TBAPF₆ dissolved in dry acetonitrile.

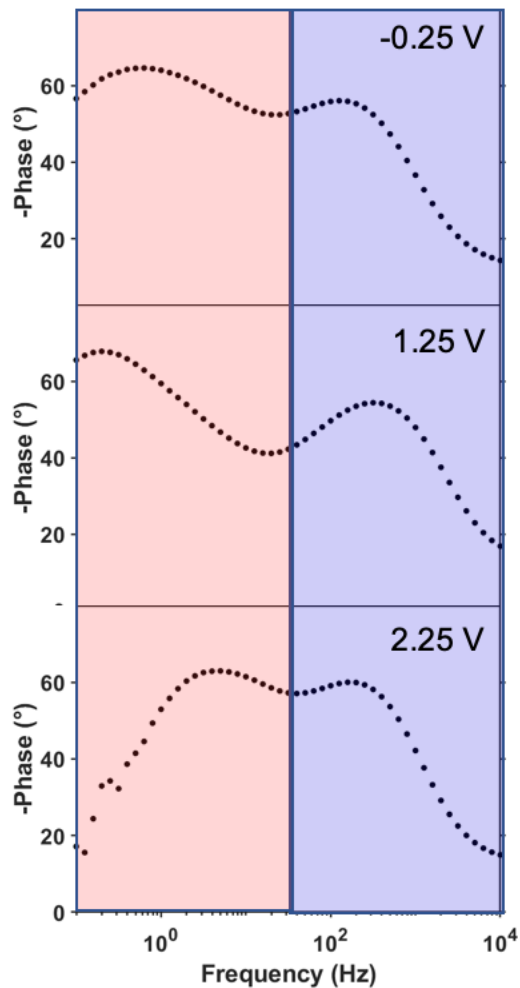


Figure S13. Representative Bode plots obtained for an electrochemically deposited NiO film immersed in 0.1 M TBAPF₆ at three different applied potentials: -0.25 V, 1.25 V, and 2.25 V versus NHE. The red and blue boxes highlight the lower and higher frequency regions of the Bode plots, respectively.

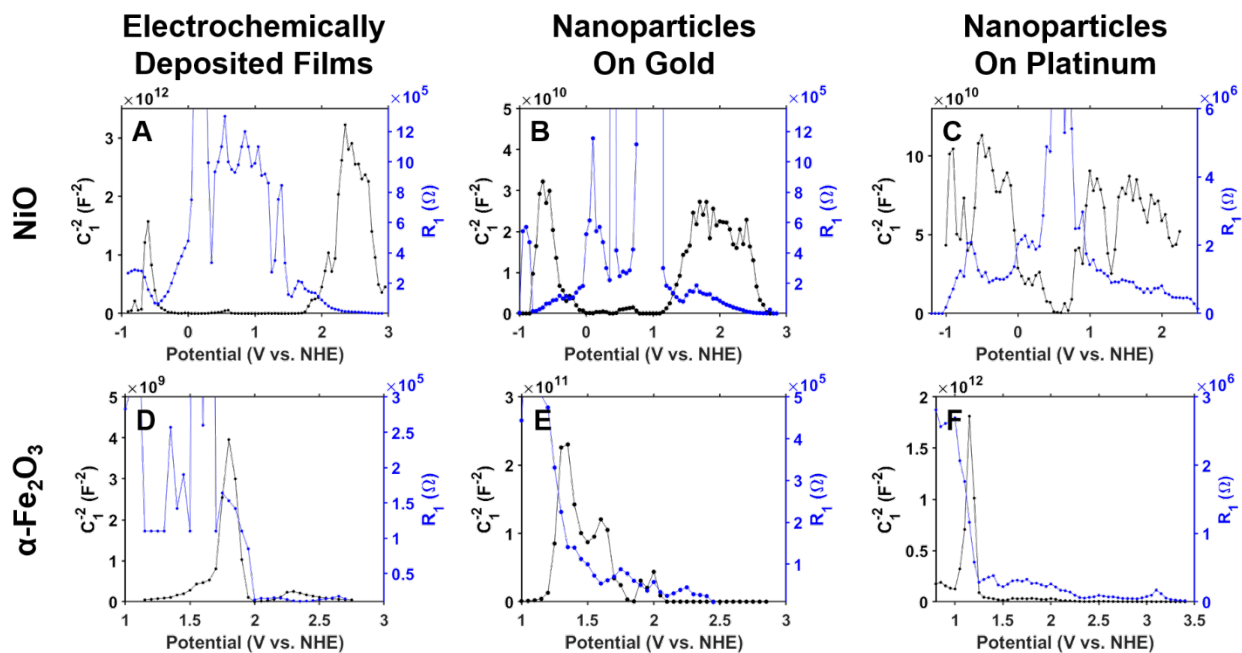


Figure S14. Plots of R_1 (blue, right axes) and $1/C_1^2$ (black, left axes) versus applied potential for films of (A) electrochemically deposited NiO, (B) NiO nanoparticles dropcast on Au, (C) NiO nanoparticles dropcast on Pt, (D) electrochemically deposited α -Fe₂O₃, (E) α -Fe₂O₃ nanoparticles dropcast on Au, and (F) α -Fe₂O₃ nanocrystals dropcast on Pt.

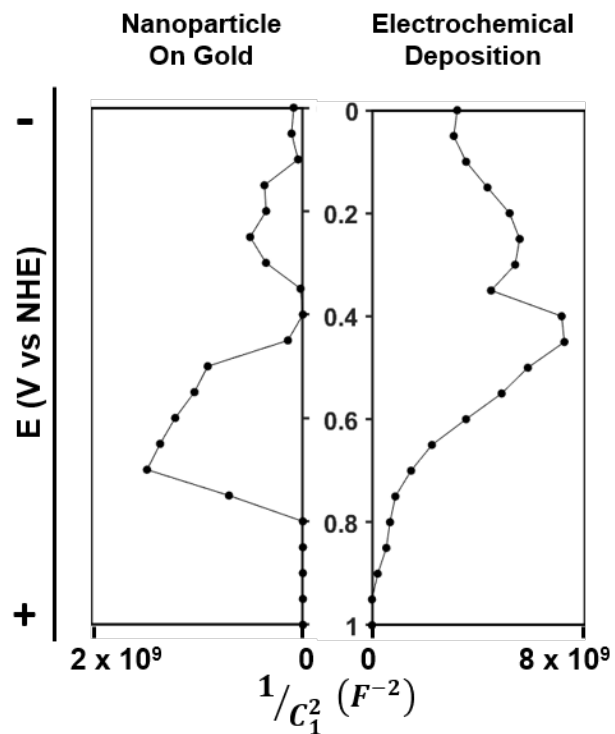


Figure S15. Plots of $1/C_1^2$ versus applied potential obtained for a film of NiO nanocrystals dropcast on Au (*left*) and an electrochemically deposited film of NiO (*right*) scaled to highlight the local maxima observed at ~ 0.7 V and ~ 0.5 V vs. NHE, respectively. These data are identical to those plotted in Figure 4 of the main text.

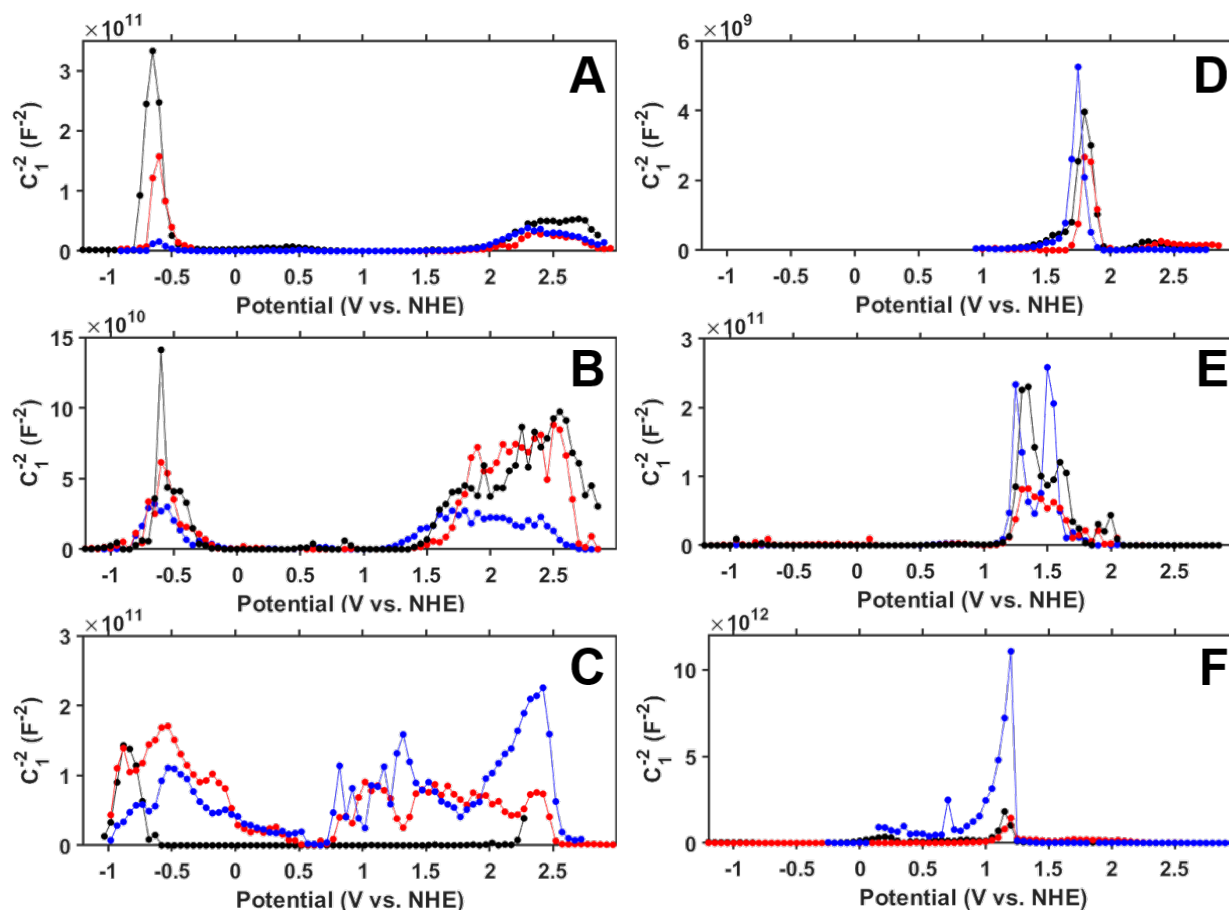


Figure S16. Plots of $1/C_1^2$ versus applied potential for (A) electrochemically deposited NiO, (B) NiO nanoparticles on Au, (C) NiO nanoparticles on Pt, (D) electrochemically deposited α -Fe₂O₃, (E) α -Fe₂O₃ nanoparticles on Au, and (F) α -Fe₂O₃ nanoparticles on Pt. These data were collected for three different films (trial 1 black, trial 2 red, and trial 3 blue) of each film type and measured in a 0.1 M solution of TBAPF₆ in acetonitrile.

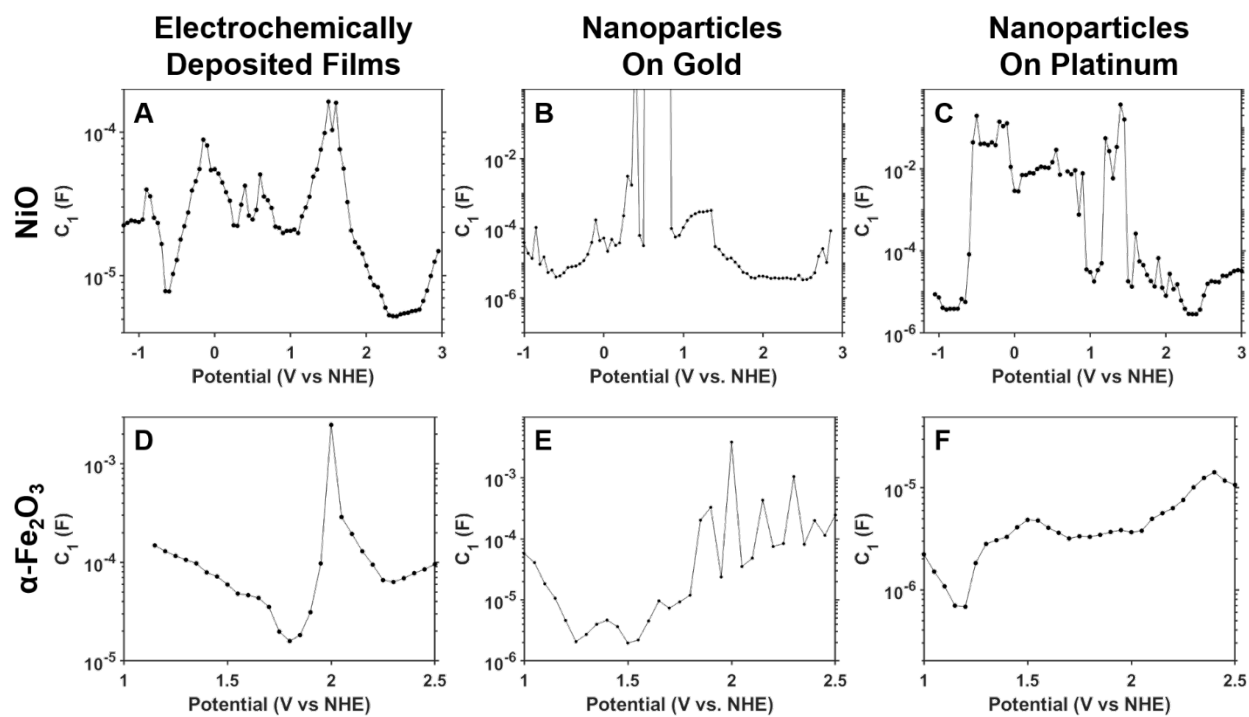


Figure S17. Plots of C_1 versus applied potential obtained for films of (A) electrochemically deposited NiO, (B) NiO nanoparticles dropcast on Au, (C) NiO nanoparticles dropcast on Pt, (D) electrochemically deposited α -Fe₂O₃, (E) α -Fe₂O₃ nanoparticles dropcast on Au, and (F) α -Fe₂O₃ nanocrystals dropcast on Pt.

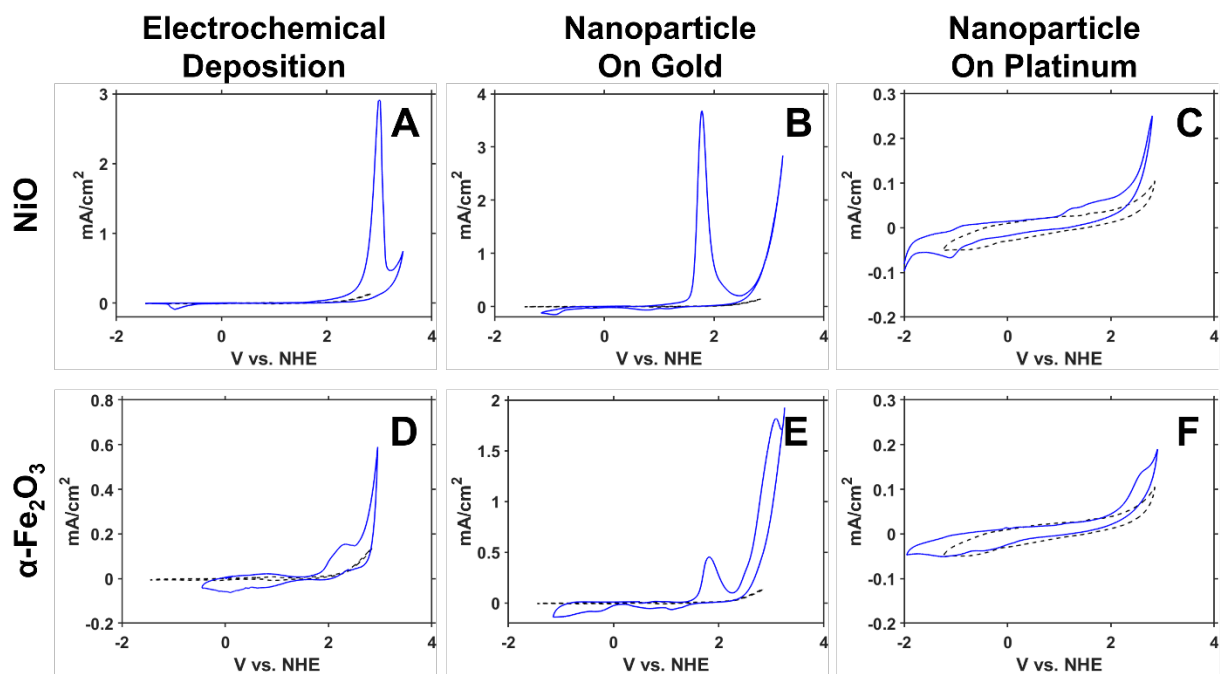


Figure S18. Representative cyclic voltammograms in 0.1 M TBAPF₆ for relevant working electrodes (A) electrochemically deposited NiO, (B) NiO nanoparticles on Au, (C) NiO nanoparticles on Pt, (D) electrochemically deposited α -Fe₂O₃, (E) α -Fe₂O₃ nanoparticles on Au, and (F) α -Fe₂O₃ nanoparticles on Pt. The dashed black lines plot cyclic voltammograms collected of the bare Au or Pt electrodes in 0.1 M TBAPF₆.

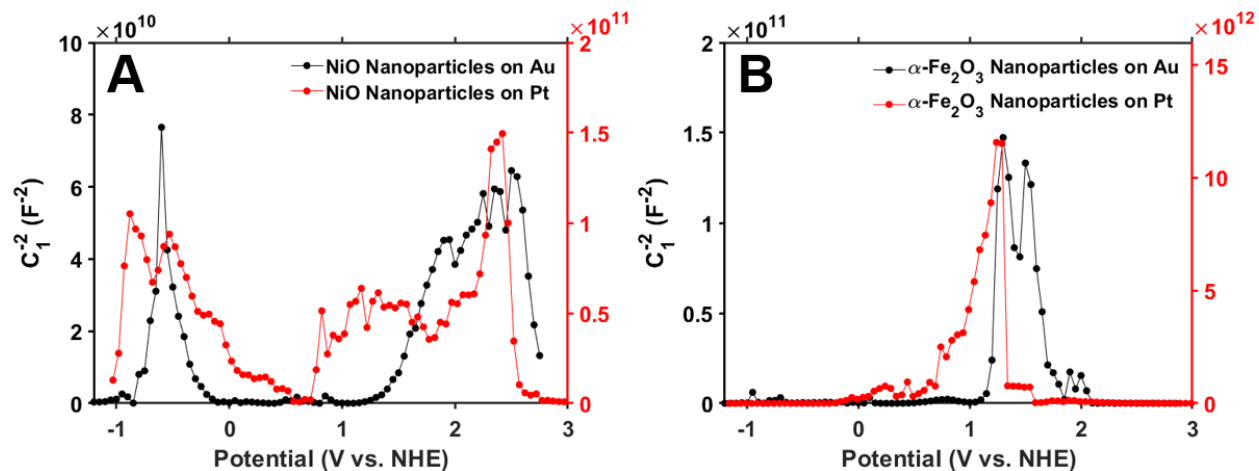


Figure S19. A) Plot of $1/C_1^2$ versus applied potential obtained for films of NiO nanoparticles dropcast onto a gold (black circles, left axis) or platinum electrode (red circles, right axis). B) Plot of $1/C_1^2$ versus applied potential obtained for films of $\alpha\text{-Fe}_2\text{O}_3$ nanoparticles dropcast onto a gold (black circles, left axis) or platinum electrode (red circles, right axis). The observed shift in the potentials at which $1/C_1^2$ reaches local maxima when the electrode changes from gold to platinum is consistent with Schottky behavior at the metal/metal oxide interface.

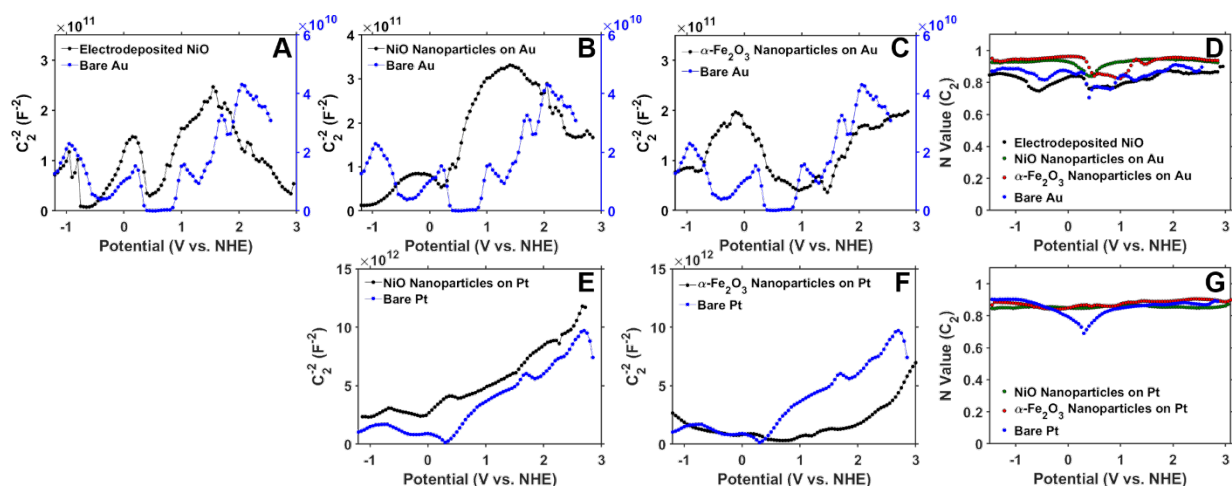


Figure S20. Comparison of C_2 parameters obtained from Circuit A fits of EIS data collected for films of NiO and α -Fe₂O₃ to C_2 parameters obtained from Circuit B fits of EIS data collected for bare gold or platinum electrodes. A 0.1 M solution of tetrabutylammonium hexafluorophosphate in acetonitrile was used as the electrolyte solution for these measurements. **A,B,C,E,F**) Representative plots of $1/C_2^2$ versus applied potential for **(A)** a film of NiO electrochemically deposited onto gold (black circles, left axis) compared to a bare gold electrode (blue circles, right axis), **(B)** a film of NiO nanoparticles dropcast onto a gold slide (black circles, left axis) compared to a bare gold electrode (blue circles, right axis), **(C)** a film of α -Fe₂O₃ nanoparticles dropcast onto a gold slide (black circles, left axis) compared to a bare gold electrode (blue circles, right axis), **(E)** a film of NiO nanoparticles dropcast onto a platinum disc (black circles) compared to a bare platinum disc (blue circles), and **(F)** a film of α -Fe₂O₃ nanoparticles dropcast onto a platinum disc (black circles) compared to a bare platinum disc (blue circles). **D,G**) Plots of the value of the N exponent obtained from fitting C_2 to a constant phase element versus applied potential for **(D)** films of NiO electrochemically deposited onto gold (black circles), NiO nanoparticles dropcast onto gold (green circles), and α -Fe₂O₃ nanoparticles dropcast onto gold (red circles) compared to a bare gold electrode (blue circles) and **(G)** films of NiO (green circles) and α -Fe₂O₃ (red circles) nanoparticles dropcast onto a platinum disc electrode and a bare platinum disc (blue circles).

Table S2. Summary of important values from the cyclic voltammograms of 1 mM ferrocene for each variable @ Au and variable @ Pt electrode shown in Figure S21. ΔE refers to the difference in potential between the anodic and cathodic peaks, which is expected to be ~ 59 mV for an ideal, reversible redox couple. Note that electrochemically deposited NiO @ Au electrodes show an extreme deviation from Nernstian behavior. i_p^+ refers to the peak cathodic current, reported in Amperes. The active electrochemical working area, A, is calculated from i_p^+ using the Randles-Sevcik equation (equation S1), with $n = 1$ for the one-electron ferrocene redox couple.^{3,4}

		<i>Scan Rate (V/s)</i>						
		0.5	0.25	0.1	0.075	0.05	0.025	
<i>Bare Metal Electrodes</i>	Au	ΔE (V)	0.125	0.105	0.083	0.078	0.78	0.073
		i_p^+ (A)	2.4×10^{-4}	1.7×10^{-4}	1.1×10^{-4}	9.7×10^{-5}	7.8×10^{-5}	5.3×10^{-5}
		A (cm ²)	27.51	28.67	29.39	29.11	28.76	27.52
	Pt	ΔE (V)	0.076	0.071	0.068	0.066	0.066	0.068
		i_p^+ (A)	1.7×10^{-5}	1.3×10^{-5}	7.9×10^{-6}	6.8×10^{-6}	5.5×10^{-6}	3.9×10^{-6}
		A (cm ²)	2.03	2.07	2.05	2.05	2.04	2.01
<i>Electrochemically Deposited Electrodes</i>	NiO	ΔE (V)	0.706	0.627	0.527	0.496	0.430	0.359
		i_p^+ (A)	2.7×10^{-5}	3.2×10^{-5}	3.3×10^{-5}	3.1×10^{-5}	3.0×10^{-5}	2.5×10^{-5}
		A (cm ²)	3.16	5.23	8.49	9.40	11.21	13.06
	α-Fe₂O₃	ΔE (V)	0.137	0.129	0.127	0.127	0.139	0.115
		i_p^+ (A)	5.1×10^{-5}	4.6×10^{-5}	3.8×10^{-5}	3.6×10^{-5}	3.0×10^{-5}	2.5×10^{-5}
		A (cm ²)	5.95	7.59	9.92	10.67	11.08	13.06
<i>Nanoparticles Dropcast on Au</i>	NiO	ΔE (V)	0.115	0.107	0.100	0.098	0.093	0.088
		i_p^+ (A)	1.1×10^{-4}	9.2×10^{-5}	7.1×10^{-5}	6.6×10^{-5}	5.8×10^{-5}	4.5×10^{-5}
		A (cm ²)	13.13	15.19	18.51	19.87	21.24	23.16
	α-Fe₂O₃	ΔE (V)	0.105	0.090	0.081	0.081	0.078	0.073
		i_p^+ (A)	1.6×10^{-4}	1.2×10^{-4}	8.2×10^{-5}	7.3×10^{-5}	6.0×10^{-5}	4.2×10^{-5}
		A (cm ²)	18.92	20.21	21.42	21.78	22.00	21.94
<i>Nanoparticles Dropcast on Pt</i>	NiO	ΔE (V)	0.095	0.088	0.088	0.085	0.085	0.081
		i_p^+ (A)	2.1×10^{-5}	1.6×10^{-5}	1.1×10^{-5}	1.0×10^{-5}	8.9×10^{-6}	7.0×10^{-6}
		A (cm ²)	2.48	2.65	2.94	3.08	3.29	3.66
	α-Fe₂O₃	ΔE (V)	0.095	0.105	0.120	0.120	0.122	0.117
		i_p^+ (A)	2.0×10^{-6}	1.7×10^{-6}	1.5×10^{-6}	1.4×10^{-6}	1.4×10^{-6}	1.2×10^{-6}
		A (cm ²)	0.23	0.27	0.38	0.43	0.50	0.65

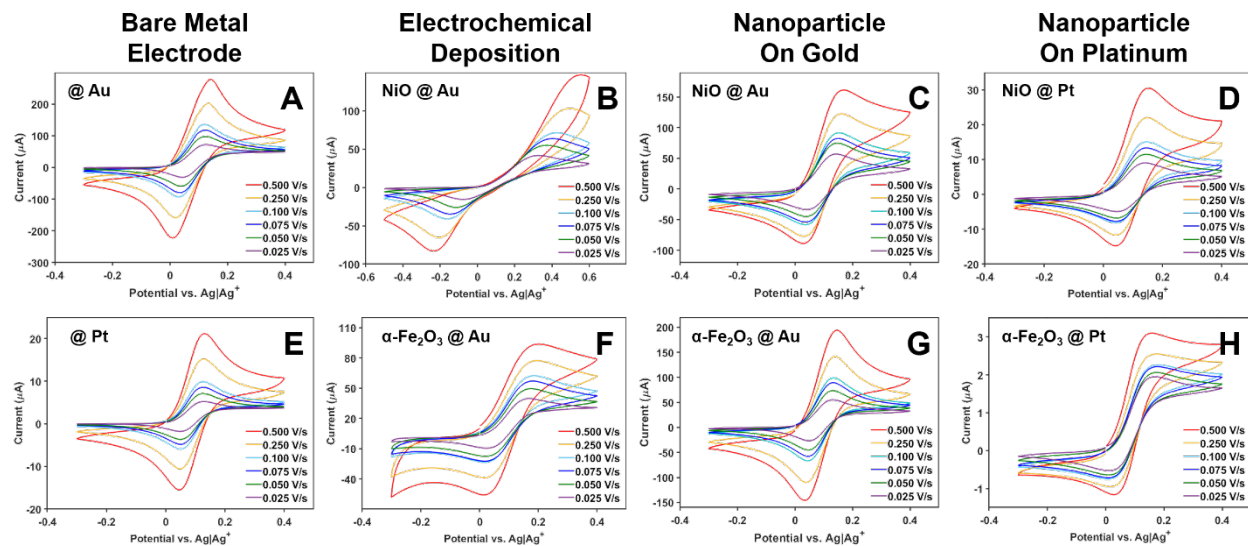


Figure S21. Representative cyclic voltammograms of 1mM ferrocene redox couple in 0.1 M TBAPF₆ for relevant working electrodes **(A)** Bare Au, **(B)** electrochemically deposited NiO, **(C)** NiO nanoparticles on Au, **(D)** NiO nanoparticles on Pt, **(E)** Bare Pt, **(F)** electrochemically deposited $\alpha\text{-Fe}_2\text{O}_3$, **(G)** $\alpha\text{-Fe}_2\text{O}_3$ nanoparticles on Au, and **(H)** $\alpha\text{-Fe}_2\text{O}_3$ nanoparticles on Pt.

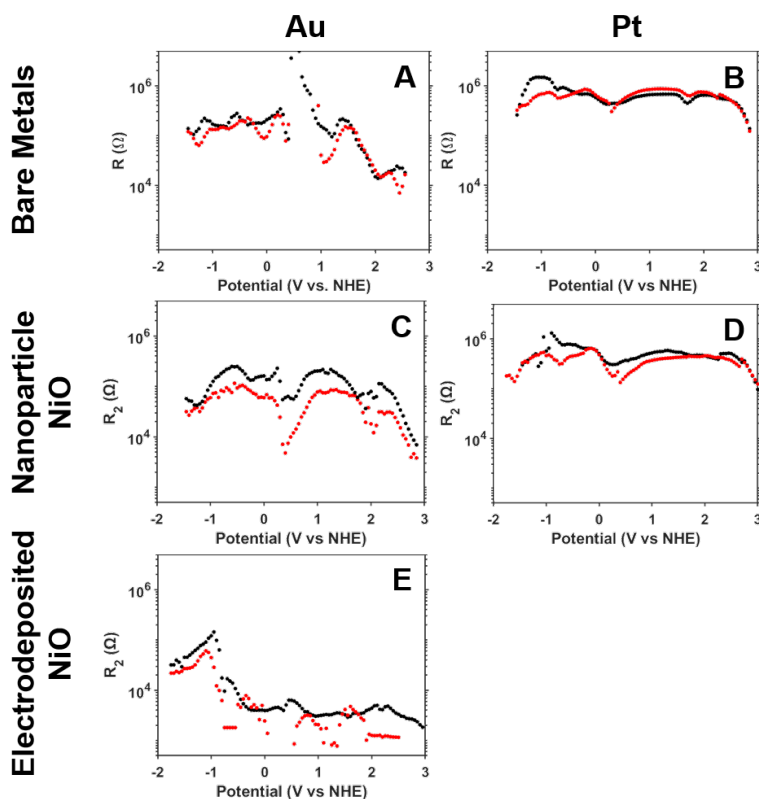


Figure S22. Plots of R_2 versus applied potential obtained for (A) a bare Au electrode, (B) a bare Pt electrode, (C) a film of NiO nanocrystals dropcast onto a Au electrode, (D) a film of NiO nanocrystals dropcast onto a Pt electrode, and (E) a film of NiO electrochemically deposited onto a Au electrode. Each plot contains data collected in 0.1 M acetonitrile solutions of TBAPF₆ (black circles) and TMAPF₆ (red circles). The R_2 values for the metal oxide films are obtained from fits of EIS data to circuit A whereas the R_2 values for the bare electrodes are obtained from fits to circuit B.

Table S3. Average Values of R_2 Obtained from EIS Measurements of Various Electrodes in Figure S22^a

	Bare Pt	Bare Au	NiO NP on Pt	NiO NP on Au	NiO EDep on Au
TMAPF ₆ ^b	6.3×10^5	1.1×10^5	3.6×10^5	5.0×10^4	9.9×10^3
TBAPF ₆ ^c	6.8×10^5	2.9×10^5	5.0×10^5	1.2×10^5	1.7×10^4

^aAll values given in ohms. ^bMeasurements performed in 0.1 M acetonitrile solution of TMAPF₆. ^cMeasurements performed in 0.1 M acetonitrile solution of TBAPF₆

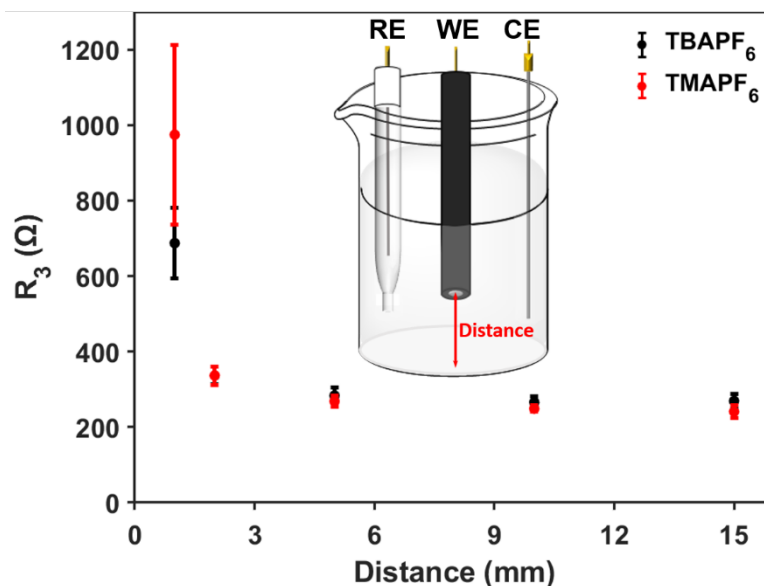


Figure S23. Resistance values (R_3 , average over three trials) plotted versus distance of bare platinum disc from the bottom of beaker (illustrated by inset image; WE = working electrode, RE = reference electrode, and CE = counter or auxiliary electrode). For both 0.1 M TBAPF₆ (black) and 0.1 M TMAPF₆ (red) electrolyte solutions, the resistance decreases with increasing distance between the Pt working electrode and the bottom of the beaker, which corresponds to increasing pathlength between the working and counter electrodes. We observe a maximum resistance at disc distance of ~1 mm: ~700 Ω for TBAPF₆ and ~1000 Ω for TMAPF₆ solutions. At larger distances, resistance values for both electrolytes reach a general equilibrium with values around ~270 Ω. All trials are measured at 0 V vs Ag/Ag⁺ reference electrode with a platinum wire counter electrode, and each electrolyte had three separate trials performed with fresh electrolyte solutions.

Table S4. Table summarizing the value of Z' corresponding the highest frequency of the oscillating applied voltage (10,000 Hz) for each Nyquist plot shown in Figure 7 in the main text.

<i>System</i>	<i>Bare Electrodes</i>		<i>α-Fe₂O₃</i>		<i>NiO</i>	
	TMA (Ω)	TBA (Ω)	TMA (Ω)	TBA (Ω)	TMA (Ω)	TBA (Ω)
<i>1</i>	62	71	73	82	68	89
<i>2</i>	101	111	157	143	126	139
<i>3</i>	340	312	400	357	312	391

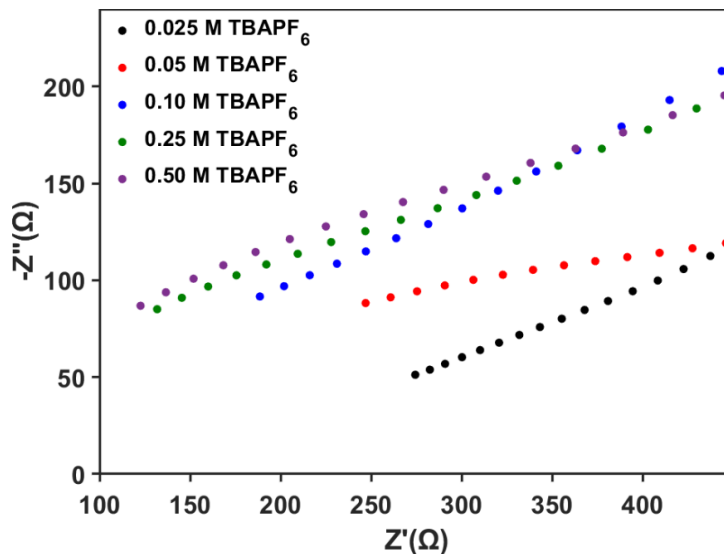


Figure S24. Representative Nyquist plots collected for an electrochemically deposited hematite film immersed in acetonitrile solutions with varied concentrations of 0.025 (black circles), 0.05 (red circles), 0.10 (blue circles), 0.25 (green circles), and 0.5 (purple circles) M tetrabutylammonium hexafluorophosphate. These results indicate that increased concentration decreases initial resistance correlated to the R_3 .

Table S5. Table summarizing the values of Z' and $-Z''$ obtained at the highest modulation frequency (10,000 Hz) for the various concentrations of TBAPF₆ illustrated in Figure S24. Values for Z' demonstrate an inverse relationship for concentration to resistance. Values for $-Z''$ show consistent resistance values, aside from the lowest concentration which likely deviates due to poor ion migration from the applied electric field.

<i>Concentration (M)</i>	<i>Concentration Dependence</i>	
	<i>Z' (Ω)</i>	<i>-Z'' (Ω)</i>
<i>0.025</i>	274	51
<i>0.05</i>	247	88
<i>0.1</i>	189	92
<i>0.25</i>	132	85
<i>0.5</i>	123	87

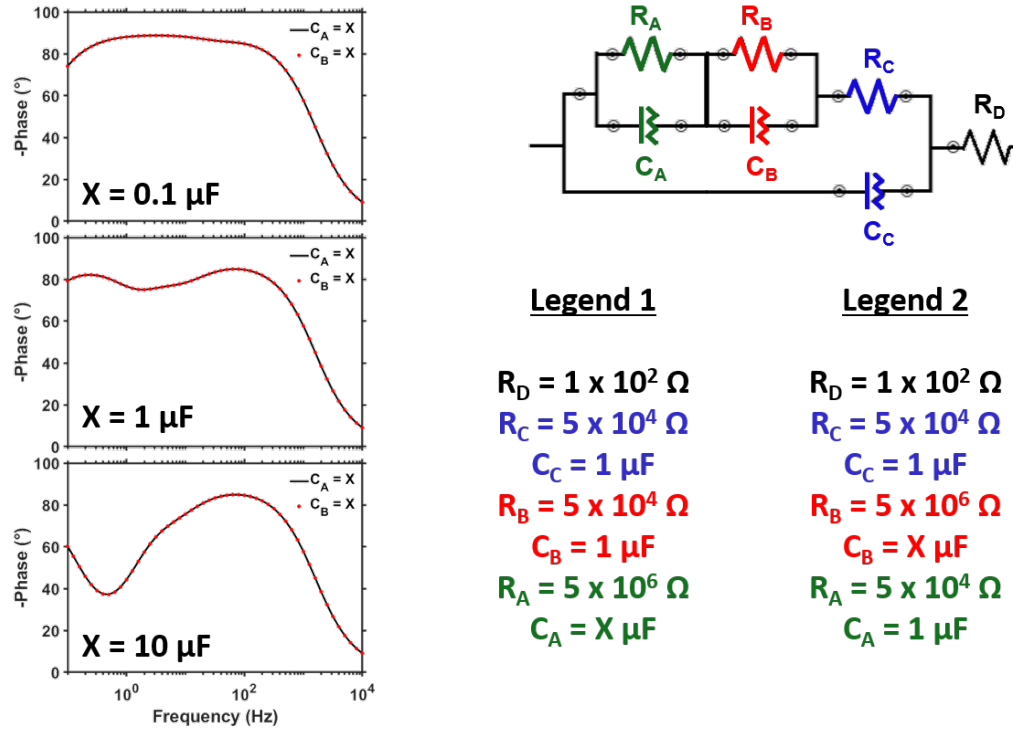


Figure S25. Simulated Bode plots (*left*) for model Circuit C (*top right*), which is similar to Circuit A with an added RC element in series with the other nested RC element (see Figure 1 from the main text). The solid black Bode plots correspond to the values for the circuit elements listed in Legend 1 and the Bode plots depicted as red circles correspond to the circuit element values listed in Legend 2. The fact that the red circles overlay exactly the black lines demonstrates that the two nested RC components (R_A/C_A and R_B/C_B) are interchangeable.

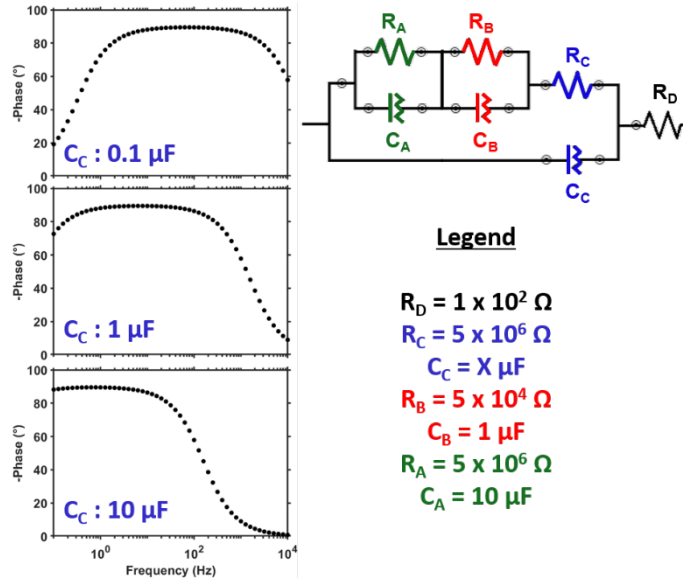


Figure S26. Simulated Bode-phase plots for model Circuit C (top right), which is similar to Circuit A with an added RC element in series with the other nested RC element (see Figure 1 from the main text). The simulated plots demonstrate that when the magnitude of the un-nested resistor (R_C) is much greater than either or both nested resistors (R_A and R_B) only a single feature can be resolved independent of the magnitude of the capacitance in parallel (C_C). Note: all capacitive elements are simulated with a value of $n = 1$.

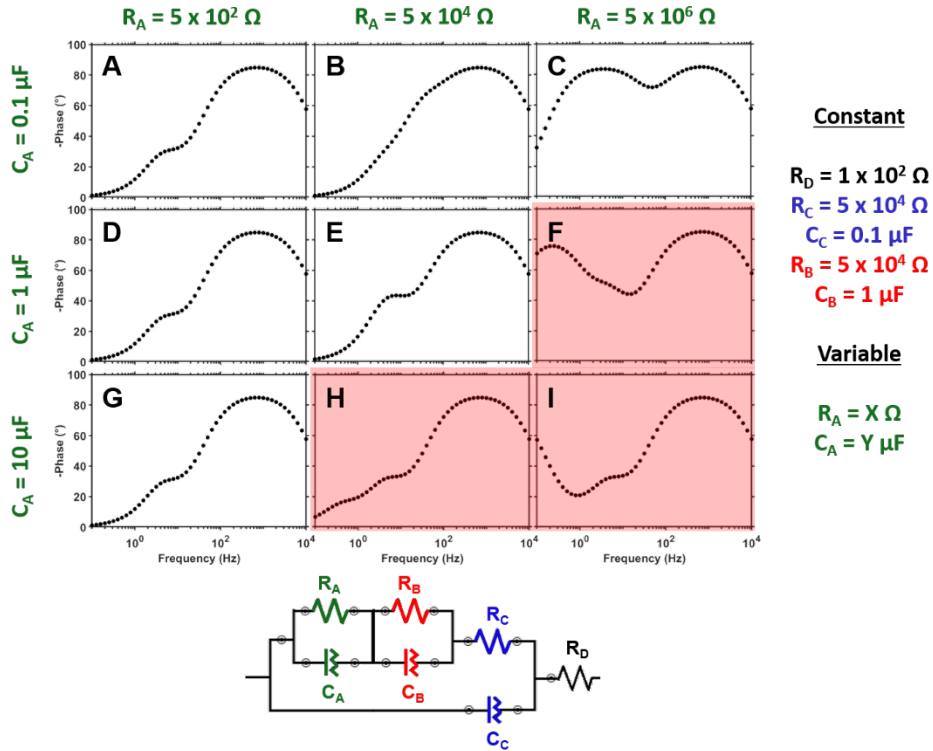


Figure S27. A-I) Simulated Bode-phase plots for model Circuit C (bottom middle), which is similar to Circuit A with an added RC element in series with the other nested RC element (see Figure 1 from the main text). The simulated plots highlighted in red demonstrate that only when the values of $R_A > R_B$ and/or $C_A > C_B$ can three separate features be resolved within a Bode plot.

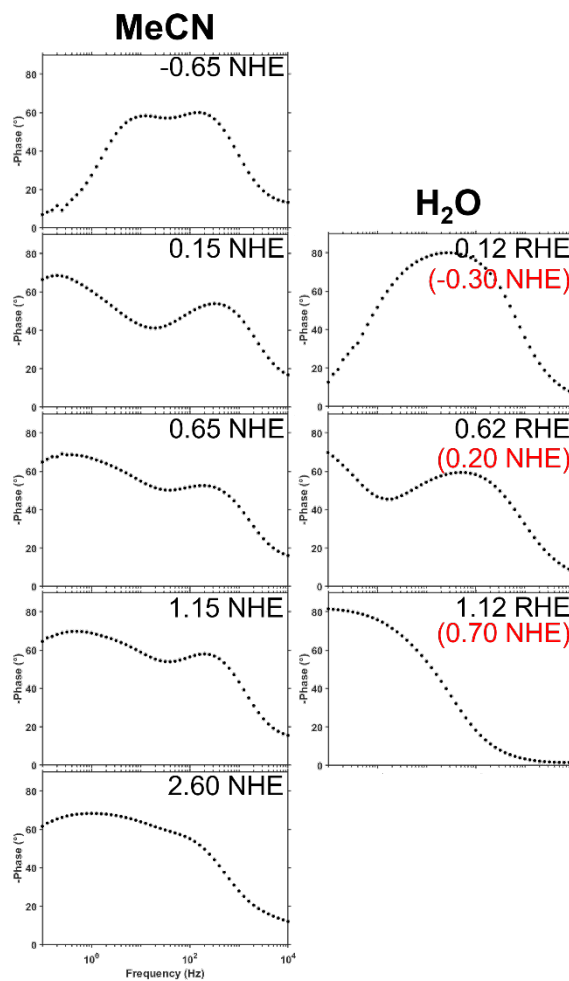


Figure S28. Representative Bode plots for NiO films electrochemically deposited on gold as analyzed in 0.1 M TBAPF₆ in MeCN (left) and 0.1 M KP_i (pH = 7.2) in water (right). Data collected in MeCN clearly shows two features throughout the entire electrochemical window which do not change drastically with potential. Data collected in water shows only one feature for potentials more negative than 0.57 vs RHE and more positive than 0.77 vs RHE which varies throughout the whole electrochemical window. The applied potentials used for these data are shown in the upper left corner of each plot. These potentials were converted from Ag|AgCl using equations S2 (for RHE) and S3 (for NHE).

References

1. M. C. Biesinger, B. P. Payne, A. P. Grosvenor, L. W. M. Lau, A. R. Gerson and R. S. C. Smart, *Appl. Surf. Sci.*, 2011, **257**, 2717-2730.
2. D. A. Brewster, Y. Bian and K. E. Knowles, *Chem. Mater.*, 2020, **32**, 2004-2013.
3. N. Elgrishi, K. J. Rountree, B. D. McCarthy, E. S. Rountree, T. T. Eisenhart and J. L. Dempsey, *J. Chem. Educ.*, 2018, **95**, 197-206.
4. A. J. Bard and L. R. Faulkner, *Electrochemical Methods: Fundamentals and Applications*, 2nd Edition, Wiley Textbooks, 2000.